Evolution and Forcing Mechanisms of El Niño over the Last 21,000 Years

Zhengyu Liu[1,2,]*, Zhengyao Lu[2], Xinyu Wen[2],

B. L. Otto-Bliesner[3], A. Timmermann[4], K. M. Cobb[5]

1. *Dept. Atmospheric and Oceanic Sciences & Nelson Center for Climatic Research, Univ. of Wisconsin-Madison, Madison, WI53706, USA*

2. *Lab. Climate, Ocean and Atmosphere Studies, School of Physics, Peking Univ., Beijing, 100871, P. R. China*

3. *Climate and Global Dynamics Division, National Center for Atmospheric Research, Boulder, CO 80307-3000, USA*

4. *IPRC and Dept. Oceanography, SOEST, University of Hawaii at Manoa, Honolulu, HI 968222, USA*

5. *School of Earth and Atmospheric Sciences, Georgia Institute of Technology, Atlanta, GA30332, USA*

*** Corresponding Author: Zhengyu Liu, Dept. Atmospheric and Oceanic Sciences & Center for Climatic Research, 1225 W. Dayton St., Madison, WI 53706, 608-262-0777 (Phone), 608-263-4190 (Fax), Email: zliu3@wisc.edu

The El Niño-Southern Oscillation (ENSO) is earth's dominant source of interannual climate variability. Yet, ENSO's response to global warming remains highly uncertain[1]. To improve our understanding of ENSO's sensitivity to external climate forcing, it is paramount to determine its past behavior using paleo climate data and model simulations. Paleo climate records document that ENSO has varied considerably since the Last Glacial Maximum (LGM, 21,000 years ago, or 21 ka)[2-9] and some datasets suggest a gradual intensification of ENSO for the past ~6,000 years[2,5,7,8]. Previous attempts to simulate the transient evolution of ENSO have relied on simplified models[10] or snapshot[11-13] experiments. Here we analyze a series of transient Coupled General Circulation Model (CGCM) simulations forced by changes in greenhouse gasses, orbital forcing and the ice-sheet history throughout the last 21,000 years. Consistent with most paleo ENSO reconstructions, our model simulates an orbitally-induced strengthening of ENSO during the Holocene, which is caused by increasing positive ocean-atmosphere feedbacks. During the early deglaciation, ENSO characteristics change drastically in response to meltwater discharges and the resulting changes of the Atlantic Meridional Overturning Circulation (AMOC) and equatorial annual cycle. Increasing deglacial atmospheric CO_2 concentrations tend to weaken ENSO, whereas retreating glacial ice-sheets intensify ENSO. The complex evolution of forcings and ENSO feedbacks and the uncertainties in the reconstruction further highlight the challenge and opportunity for constraining future ENSO responses.

To understand ENSO's evolution during the past 21,000 years, we analyze the baseline transient simulation (TRACE) conducted with the Community Climate System model version 3 (CCSM3). This simulation utilizes the complete set of realistic climate forcings: orbital, greenhouse gases, continental ice sheets and meltwater discharge (Figs.1a, d; Methods text 1). TRACE has been

shown to replicate many key features of the global climate evolution[14,15]. Over the tropical Pacific, the annual mean sea surface temperature (SST) closely tracks atmospheric CO_2 (Fig.1d); the cross-equatorial eastern Pacific meridional SST gradient largely tracks the meltwater forcing and the resulting AMOC change, consistent with proxy evidence[15] (Figs.1b, c). ENSO amplitude changes in a complex pattern, as seen in the interannual SST variability over the central-eastern Pacific (Fig.1e, Methods text 2, Extended Data Fig.1). In 100-year windows, ENSO amplitude varies considerably on a multitude of timescales (Extended Data Fig.2a), similar to those in other multi-millennial simulations[16] and in paleo-ENSO reconstructions from lake sediments[2, 7, 17] (Fig.1e) and fossil corals[6] from ENSO-teleconnected regions. The unforced variance changes of ENSO may originate from the nonlinear dynamics of ENSO[10] and/or stochastic climate forcings[18,19].

Beyond the background irregularity of ENSO amplitude, however, there are externally forced changes (Fig.1e, Extended Data Fig.2a), such as a reduction in ENSO amplitude just after the LGM before leveling off during the Heinrich Stadial 1 (HS1, ~17ka), a rapid weakening related to the AMOC resumption at the onset of the Bølling-Allerod (BA, ~14.5 ka) and an increase during the Younger Dryas (YD, ~12.9-11.7ka). During the Holocene, ENSO gradually intensifies by ~15%. The simulated ENSO evolution is qualitatively similar to that in other models at 6ka and 21ka, falling within the spread of PMIP2/PMIP3 ensemble[20] (Fig.1e).

The simulated ENSO intensification over the Holocene is qualitatively consistent with several key ENSO-sensitive proxy records (Fig.1e), such as the increase of precipitation variability along the South America coast throughout the Holocene[2,4,7] (Extended Data Figs.3a,b, 4c,d, 5c, Methods text 3), and the increase in ENSO variance in the western Pacific fossil corals from the mid- to late-Holocene[3]. An intensification of ENSO during the Holocene is also inferred from the ensemble spread of SST from foraminifera in the eastern Pacific[5], although this

ensemble spread likely reflects more the total SST variability, which is dominated by the annual cycle rather than ENSO there (Fig.1f, Extended Data Fig.2b). Nevertheless, the most recent reconstructions of ENSO's evolution over the Holocene suggest that ENSO variance reached a minimum around mid-Holocene[5,6,21] (Fig.1f, Extended data Fig.6b), with a reduction of ~30-50% relative to the late Holocene. Such a trajectory is not inconsistent with previously published paleo-ENSO datasets, given their small sample size relative to the high level of intrinsic variability in ENSO amplitudes (Method text 4, Extended Data Figs. 2b, c, 6).

The simulated trend in NINO3.4 variance over the Holocene amounts to +15%, consistent with the majority of mid-Holocene PMIP2/PMIP3 experiments, which exhibit increases of 10-15% in ENSO variance from 6ka to pre-industrial conditions[20] (Fig.1e). If the response of ENSO to precessional forcing was indeed relatively modest as in current models, the available paleo-ENSO datasets are as yet too sparse to detect such a subtle shift in the Holocene, given the high level of background variability[6] (Method text 4). If, on the other hand, ENSO did have intensified by 50% and did reach the minimum in the mid-Holocene, the inconsistent simulations in current models would imply model deficiencies. The ultimate resolution of the detailed evolution characteristics of ENSO variance in the Holocene requires much more high-resolution paleoclimate data from ENSO centers of action in the future.

The comparison with observations prior to the Holocene poses an even deeper challenge because proxy records of ENSO are rare and less consistent. The few coral records scattered across the last glacial period suggest an active ENSO presence[3, 22], but the coral records are too short and sparse to provide a robust estimation of ENSO intensity changes[6] (Methods text 4). Other records seem to show conflicting results. The lithic flux rate associated with flood events in a sediment record off Peru has been used to argue for the change of ENSO-related flooding event, which is weaker at LGM than late Holocene[8], as also implied by a varve record in East

Africa[17]. The lithic flux data further infer that ENSO intensified rapidly from 17 to 13ka before gradually peaking at 8ka[8]. However, the variability of eastern equatorial Pacific subsurface temperatures reconstructed from subsurface dwelling planktonic foraminifera suggests a modestly stronger ENSO at LGM, which then intensifies to peak at 15ka and then weakens towards the minimum at 8ka[9]. The PMIP2/PMIP3 experiments also show a wide spread of ENSO's response at LGM with no statistically significant change of the ensemble mean ENSO at LGM relative to late Holocene[20]. The ENSO amplitude in TRACE is reduced by ~0.2°C at LGM relative to late Holocene, well within the spread of the PMIP2/PMIP3 experiments (Fig.1e). The inconsistent ENSO responses during the deglaciation, among data and among models, could be caused by various reasons. The use of paleo records in remote regions as proxies for ENSO variance should be treated with caution, especially for those sites outside the region of strong ENSO impact (Methods text 3, Extended Data Figs.4a,b) where the trend of precipitation variance is dominated by the local response to deglacial climate forcings (Extended data Figs.5a,b), rather than by ENSO effects. In addition, the relation between the proxy variance and ENSO variance could change over time, as seen in the less consistent variance between precipitation and ENSO during the deglaciation than the Holocene (Extended Data Figs.3c-e, 5a,b, Methods text 3). The intrinsic irregularity of ENSO[16] itself also calls into question the use of snapshots of ENSO amplitude snapshots, both in paleo data and climate models, to represent the continuous evolution.

To determine the physical mechanisms that cause millennial to orbital scale changes in ENSO strength in TRACE, we quantify the time-evolution of ocean-atmosphere feedbacks in the eastern Pacific using the Bjerknes Index (BJ index), which consists of three positive feedbacks (upwelling feedback, zonal advection feedback, thermocline feedback) and two negative feedbacks (heat flux feedback, mean advection feedback)[23] (Methods text 5). In the Holocene,

both the BJ index (Fig.2d) and ENSO amplitude (Fig.2b) increase in unison (positive correlation

of 0.5, p=0.004, 10-0ka), suggesting a contribution of positive ocean-atmosphere feedback to

ENSO intensification. The BJ index increases primarily due to the upwelling feedback

(Extended Data Fig.7b). All the positive feedbacks increase throughout the Holocene via

increased wind sensitivity to SST (Extended Data Fig.8a), likely related to the warming trend in

annual mean climatology (Fig.1d) that favors active moisture convection and in turn an enhanced

atmospheric response to SST anomalies[11]. The tropical warming is forced mainly by the

increased annual mean insolation in response to the decreasing obliquity[24] and increasing CO_2.

The upwelling feedback is further amplified by the intensified upper ocean stratification

(Extended Data Fig.8f), which is generated by the increased austral winter cooling over the

subtropical South Pacific (Fig.2a) and the subsequent equatorward ventilation[12] (Methods text 5,

Extended Data Fig.9). Thus, the intensifying ENSO in the Holocene is mainly caused by

enhanced positive ocean-atmosphere feedbacks, especially the upwelling feedback, in response

to precessional forcing.

The dominant role of precessional forcing on ENSO evolution is further confirmed by a

sensitivity experiment forced by only orbital forcing (ORB, Methods text 1). The ORB

experiment almost reproduces the slow trends of ENSO (Fig.2b), annual cycle (Fig.2c) and the

BJ index (Fig.2d) in TRACE throughout the 21,000 years, except for the millennia-scale events

associated with changes of the AMOC during the early deglaciation (Figs.2b,c). Therefore, the

overall evolution of ENSO, with an initial weakening towards the early Holocene and a

subsuquent strengthening towards the late Holocene, is determined largely by the strength of

ocean-atmosphere feedback (Fig.2d) and its response to precessional forcing (Fig.2a). The

annual cycle of eastern Pacific SST also weakens towards the early Holocene and recovers

towards the late Holocene. This change of annual cycle is caused by the insolation annual cycle

in the subtropical South Pacific (Fig.1a), which forces a local annual cycle that propagates equatorward due to air-sea interactions[25]. The minimum amplitude of annual cycle in the early to mid-Holocene is also qualitatively consistent with PMIP2/PMIP3 experiments for 6ka and LGM (Fig.2c).

In contrast to ENSO's response to precessional forcing, the millennial variability of ENSO's intensity during the early deglaciation is caused by the changes of the annual cycle amplitude triggered by deglacial meltwater fluxes and the resulting AMOC responses. Indeed, the millennial swings of ENSO amplitude often change out-of-phase with the BJ index, notably around HS1 and YD (Figs.2b and 2d, Extended Data Fig.7a), and therefore cannot be explained by changing ocean-atmosphere instability as in the case of orbital forcing. As such, there is no significant correlation between ENSO intensity and BJ-index (0.09, p=0.58, 21-10ka). Instead, the millennial ENSO variance (Fig.2b) tends to vary out-of-phase with the amplitude of the annual cycle (Fig.2c), with a highly significant negative correlation of -0.49 (p=0.002, 21-10ka). The close ENSO-annual cycle interaction is also consistent with the strong phase-locking of ENSO during early deglaciation (Extended Data Fig.10). A meltwater pulse in the North Atlantic (Fig.1a) reduces the AMOC (Fig.1b), shifts the Intertropical Convergence Zone (ITCZ) southward and creates an equatorially more symmetric annual mean climate in the eastern equatorial Pacific, corresponding to a weaker north-south SST difference (Fig.1c) and a weaker equatorial annual cycle (Fig.2c)[26]; the weaker annual cycle then amplifies ENSO through the nonlinear mechanism of frequency entrainment[26,27]. The anti-correlation between annual cycle strength and ENSO variance has also been observed for other external forcings in many CGCMs[28]. The role of the meltwater forcing is confirmed explicitly in a transient sensitivity experiment forced by the deglacial meltwater forcing alone (MWF). In MWF, ENSO's

amplitude (Fig.3a, blue) varies largely out-of-phase with that of the annual cycle (Fig.3b, blue) at millennial time scales, similar to TRACE.

The dominant roles of precessional and meltwater forcings for the deglacial evolution of ENSO raises an important question: what is the role of CO_2 forcing on ENSO? To address this question, we analyze an additional sensitivity experiment forced by the greenhouse gases alone (CO2). In CO2, ENSO weakens gradually from 17 to 12 ka (Fig.3a), following the rising CO_2 (Fig.1c). The ENSO weakening in CCSM3 can be caused by a more diffusive equatorial thermocline forced by the CO_2 warming[29], and a more asymmetric tropical warming around the equator and in turn a stronger annual cycle (Fig.3b) through frequency entrainment[30]. This CO_2-induced ENSO weakening can be detected in TRACE as the gradual reduction of ENSO from 17ka towards the BA (~14.5ka). However, the weakening leaves little net signal after BA (Fig.3a), because of the offset by the ENSO amplification associated with the ice sheet retreat at ~14ka. As shown in another sensitivity experiment forced by the ice sheet alone (ICE), ENSO is amplified abruptly at 14ka by a large ice sheet retreat over the North America (Fig.3a). The ice sheet retreat changes the atmospheric jet and, in turn, the tropical Pacific climatology through teleconnections, which lead to a weaker equatorial annual cycle (Fig.3b, Methods text 5), and eventually a strengthening ENSO again through frequency entrainment[27]. The opposite effects of CO_2 and ice sheet on ENSO amplitude offer an explanation why, unlike the robust ENSO response in the Holocene, the response of ENSO amplitude at LGM differs among models[20]. At LGM, since the precessional forcing is similar to the late Holocene, ENSO is affected by two large forcings of the opposite effects: the lower CO_2 and the presence of large ice sheets.

Overall, the ENSO evolution reconstructed from available proxy records appears to be qualitatively consistent with the simulated ENSO strengthening during the Holocene. However,

the proxy data must be improved significantly to help better constrain climate models for the simulation of ENSO evolution in the past and, eventually, for the model projections of the future.

References

1. Mat C. et al., The impact of global warming on the tropical Pacific ocean and El Nino *Nature Geoscience* **3**, 391-397 (2010)

2. Moy, C. et al, Variability of El Niño/Southern Oscillation activity at millennial timescales during the Holocene epoch, *Nature* **420**, 162-166 (2002)

3. Tudhope, A. et al., Variability in the El Niño-Southern Oscillation through a glacial-interglacial cycle. *Science* **291**, 1511-1517 (2001).

4. Riedinger, M. et al., A ~6100 ^{14}C yr record of El Niño activity from the Galapagos islands. *J. Paleolimnol*. **27**, 1-7 (2002)

5. Koutavas, A. & Joanides, S., El Niño-Southern Oscillation extrema in the Holocene and Last Glacial Maximum. *Paleoceanography* **27**, PA4208, doi:10.1029/2012PA002378 (2012)

6. Cobb K. et al., Highly variable El Niño-Southern Oscillation throughout the Holocene. *Science* **339**, 67-70 (2013).

7. Conroy J. et al., Holocene changes in eastern tropical Pacific climate inferred from a Galapagos lake sediment record. *Quat. Sci. Rev*. **27**, 1166-1180 (2008)

8. Rein B. et al., El Niño variability off Peru during the last 20,000 years. *Paleoceanography* **20**, 4, PA4003, doi:10.1029/2004PA001099 (2005).

9. Sadekov, A. et al., Paleoclimate reconstructions reveal a strong link between El Niño-Southern Oscillation and tropical Pacific mean state. Nature Communication, *DOI:10.1038/ncomms3692* (2013)

10. Clement, A., Seager, R., Cane, M., Suppression of El Niño during the Mid-Holocene by Changes in the Earth's Orbit. *Paleoceanography* **15**, 731-737 (2000).

11. Roberts W., An Investigation into the Causes for the Reduction in the Variability of the El Niño-Southern Oscillation in the Early Holocene in a Global Climate Model. *PhD thesis, Univ. Washington,* 145 pp. (2007)

12. Liu, Z., Kutzbach, J. & Wu L., Modeling climatic shift of El Niño variability in the Holocene. *Geophys. Res. Lett*. **27**, 2265-2268 (2000).

13. Otto-Bliesner B. et al., Modeling El Niño and its tropical teleconnections during the glacial-interglacial cycle. *Geophys. Res. Lett.* **30**, doi:10.1029/2003GL08553 (2003)

14. Liu, Z. et al., Transient simulation of last deglaciation with a new mechanism for Bølling-Allerød warming. *Science,* **325**, 310-314 (2009).

15. Shakun J. et al., Global warming preceded by increasing CO_2 during the last deglaciation. *Nature*, **484**, 49-54 (2012).

16. Wittenberg, A., Are historical records sufficient to constrain ENSO simulations. *Geophys. Res. Lett.* **36**, L12702 (2009).

17. Wolff C. et al., Reduced interannual rainfall variability in East Africa during the Last Ice Age. *Science*, **333**, 743-747 (2011)

18. Penland, C. & Sardeshmukh, P., The optimal growth of tropical sea surface temperature anomalies. *J. Clim*., **8**, 1999-2024 (1995)

19. Chiang, J., Fang Y. & Chang P., Pacific Climate Change and ENSO Activity in the Mid-Holocene. *J. Clim.*, **22**, 923-939 (2009).

20. Masson-Delmotte V. et al, Ch. 5: Information from Paleoclimate Archives. In: T.F. Stocker et al. (Editors), *Climate Change 2013: The Physical Science Basis. Contribution of Working*

Group I to the Fifth Assessment Report of the Intergovernmental Panel on Climate Change, Cambridge University Press, Cambridge and New York, 383-464 (2013)

21. Carre M., et al., Holocene history of ENSO variance and asymmetry in the eastern tropical Pacific. *Science*, 345, 1045-1048 (2014)

22. Felis T. et al., Pronounced interannual variability in tropical South Pacific temperatures during Heinrich Stadial 1. *Nature Communications*, 1-7, July, 24 (2012),

23. Kim, S. & Jin, F., An ENSO stability analysis. Part I: results from a hybrid coupled model. *Clim. Dyn*., DOI 10.1007/s00382-010-0796-0 (2010)

24. Liu, Z., Brady, E. & Lynch-Steiglitz, J., Global ocean response to orbital forcing in the Holocene. *Paleoceanography* **18**, 1041, doi:10.1029/2002PA000819 (2003).

25. Liu Z. & Xie S., Equatorward propagation of coupled air-sea disturbances with application to the annual cycle of the eastern tropical Pacific. *J. Atmos. Sci.* **51**, 3807-3822 (1994).

26. Timmermann A. et al., The Influence of a Weakening of the Atlantic Meridional Overturning Circulation on ENSO. *J. Clim*., **20** 4899-4919 (2007)

27. Liu, Z. A simple model study of the forced response of ENSO to an external periodic forcing. *J. Clim*. **15**, 1088-1098 (2002).

28. Timmermann A. et al., The effect of orbital forcing on the mean Mean Climate and Variability of the Tropical Pacific. *J. Climate* **20**, 4147-4159 (2007).

29. Meehl G., H. Teng & G. Branstator, Future changes of El Nino in two global climate models. *Clim. Dyn*. **26**, 549-566 (2006)

30. Timmermann, A., Jin F. & Collins M., Intensification of the annual cycle in the tropical Pacific due to greenhouse warming. *Geophy. Res. Lett*., **31**, L12208, doi:10.1029/2004GL019442 (2004)

Acknowledgements

Author Contribution

Z. Liu conceived the study and wrote the paper, Z. Lu and XW performed the analysis, Z. Liu and BOB contributed to the simulations, AT and KC contributed to the interpretation, all authors discussed the results and provided inputs to the paper.

Author Information

Reprints and permissions information is available at www.nature.com/reprints. The authors declare no competing financial interests. Correspondence and requests for materials should be addressed to zliu3@wisc.edu.

Figure Legends
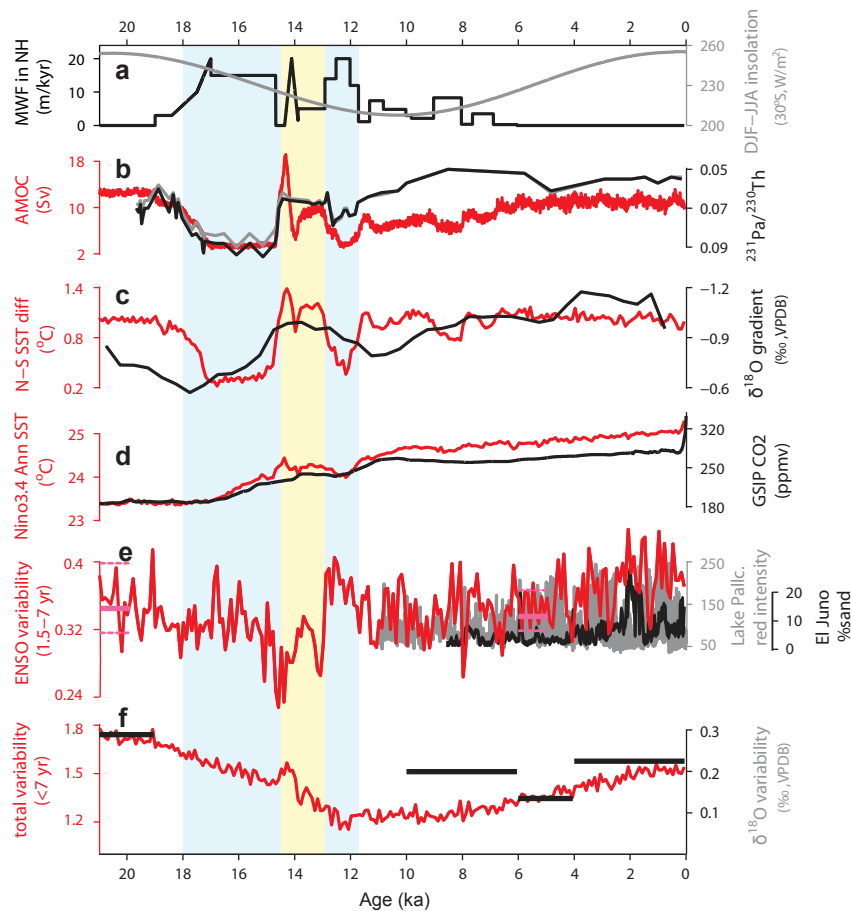
Fig.1: TRACE simulation and observation. (a) Amplitude of annual cycle of insolation (DJF-JJA) at 30^oS[31] (grey). Meltwater flux into the North Atlantic (in equivalent sea level change of m/1000-year) (black and grey). (b) AMOC transport (in Sv.=10^6 m^3/s, red) and Pa/Th ratio in Bermuda (black)[32], (c) Eastern Pacific N-S difference of annual SST (5^oN-15^oN minus 5^oS-15^oS, 140^oW-100^oW) (red) and the reconstruction (black)[5]. (d) Nino 3.4 (170^oW-120^oW, 5^oS-5^oN) annual SST (red) and CO_2 reconstruction (black)[33]. (e) ENSO amplitude [standard deviation of Nino 3.4 interannual (1.5-7 years) SST variability] in 100-year windows (red), the lake sediment records in the eastern Pacific (black)[7] and South America coast (grey)[2]. The pink bars at 6ka and 21ka represent the median (solid) and 75% and 25% pencentiles (dashes) of ENSO amplitude changes in the middle Holocene and LGM experiments in PMIP2/PMIP3 ensemble[20] (rescaled

using TRACE ENSO in the late Holocene 2-0 ka). (f) Amplitude (standard deviation) of Nino 3 (150°W-90°W, 5°S-5°N) SST total variability (< 7 years) in 100-year windows, the reconstruction of total SST variance (black bars) derived from sediment cores in the eastern equatorial Pacific[5].
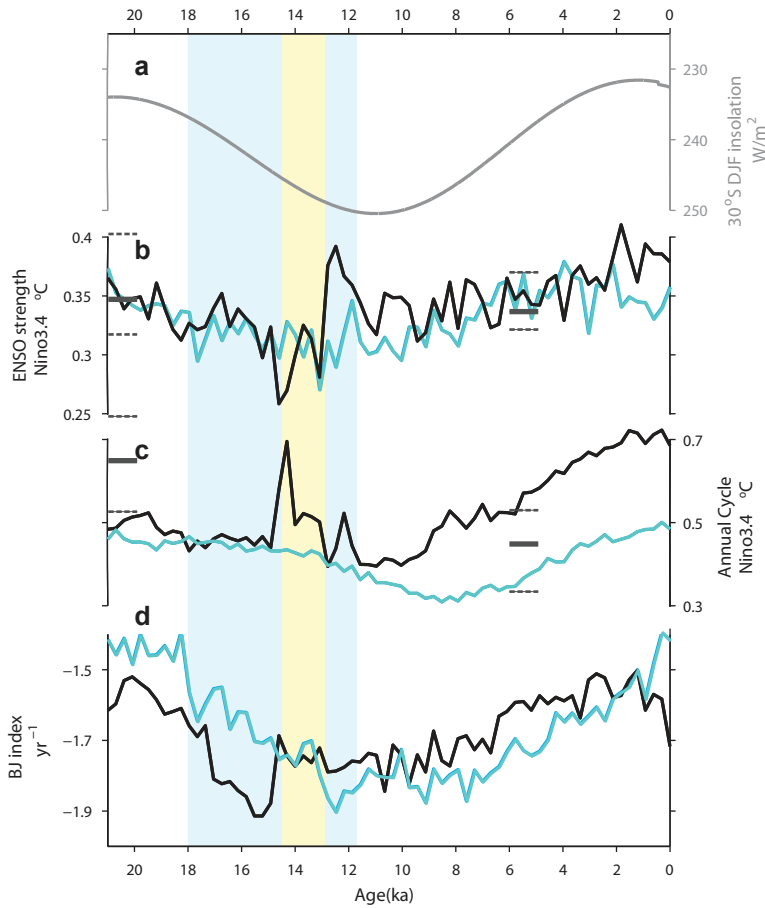
Fig.2: ENSO, Bjerknes Instability-Index and annual cycle: (a) Austral winter (JJA) insolation at 30°S. The amplitude of (b) ENSO and (c) annual cycle of Nino 3.4 SST and (d) the BJ index in the eastern equatorial Pacific (180°W-80°W, 5°S-5°N). All are calculated in 300-year windows with black for TRACE and cyan for ORB. In (b) and (c), the grey bars at 6ka and 21ka represent the median (solid) and 75% and 25% percentiles (dashes) of the amplitudes of ENSO and annual cycle in the middle Holocene and LGM experiments in PMIP2/PMIP3 ensemble[20] (rescaled using TRACE in the late Holocene 2-0ka).
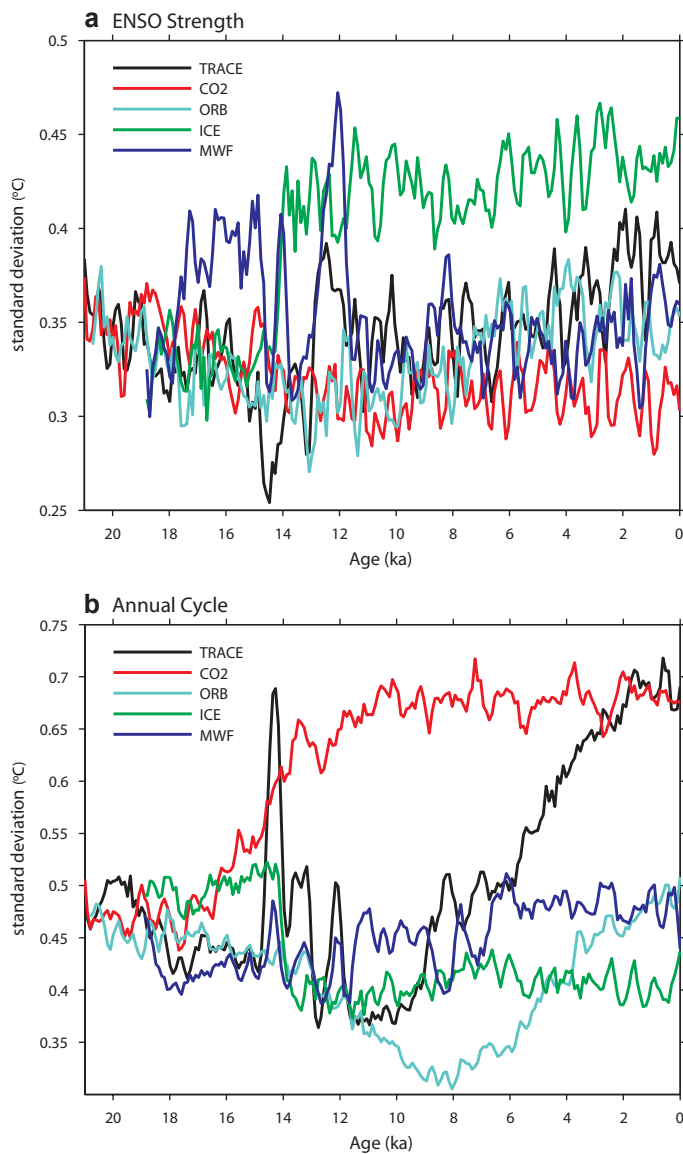
Fig.3: ENSO in single forcing experiments: Amplitude (°C) of (a) ENSO and (b) annual cycle in TRACE (black), ORB (cyan), MWF (blue), CO2 (red) and ICE (green). The amplitude is calculated as the standard deviation of Nino 3.4 SST in the frequency band of 1.5-7 years for ENSO, and for the composite seasonal cycle for annual cycle, both in 300-year windows. The natural variability of the ENSO amplitude can be estimated approximately from the Holocene part of CO2, MWF and ICE as a standard deviation of ~0.2°C.

Methods

Methods text 1: Model and Simulations

The model is the Community Climate System Model version 3 (CCSM3)[34] maintained at the National Center for Atmospheric Research (NCAR), with the resolution of T31x'3 and include a dynamic vegetation component and fixed annual cycle of aerosol forcing. As a continuation of the DGL-A simulation of ref. 14, the TRACE experiment is initialized from an equilibrium simulation forced by the LGM forcing (22 ka), and is then forced by the complete set of realistic transient climate forcing, orbital insolation[31], atmospheric greenhouse gases [32], and meltwater discharge (Fig.1b); the continental ice sheet is modified according to ICE-5G[35], once per 1,000 years for 19–17 ka, and once per 500 years after 17 ka. The coastlines and bathymetry are modified at 13.1 ka with the removal of the Fennoscandian Ice Sheet from the Barents Sea, at 12.9 ka with the opening of the Bering Strait, at 7.6 ka with the opening of Hudson Bay and finally at 6.2 ka with the opening of the Indonesian Throughflow. Meltwater fluxes are derived largely follow the record of sea level rise and geological indicators of ice sheet retreat and meltwater discharge. The meltwater forcing during mwp-1A consists of contributions from the Antarctic (15 m of equivalent sea-level volume) and Laurentide (5 m of equivalent sea-level volume) Ice Sheets (see ref. 36 for more details).

Four single forcing experiments are integrated the same as TRACE, but each is forced by a single transient forcing only with other forcings fixed at conditions at the start of each simulation[37]. The ORB and CO2 runs are initialized from the TRACE state at 22 ka; the ORB is forced by only the transient orbital forcing, and GHG forced by only the transient greenhouse gas concentrations after 22ka. The MWF and ICE are initialized at the TRACE state of 19ka; the MWF is forced by only the transient Northern Hemisphere meltwater fluxes and ICE forced by the changing continental ice-sheet after 19ka.

Methods text 2: Model ENSO

ENSO simulated by the model for present exhibits many realistic features, although the ENSO period tends to be biased towards quasi-biannual, as opposed to a broader 2-7 year peak in the observation[38]. The ENSO mode resembles the SST mode[29] and propagates westward as in many CGCMs. In the last 21,000 years, the preferred period of model ENSO remains at quasi-biannual with the power spectrum changing only modestly with time (Extended Data Fig.1).

Methods text 3: The use of remote precipitation variability to infer the change of ENSO

ENSO's is defined normally in terms of the interannual SST variance in the central-eastern equatorial Pacific region, typically the Nino 3.4 (170°W-120°W, 5°S-5°N) or Nino 3 (150°W-90°W, 5°S-5°N) region. A direct measurement of ENSO's amplitude therefore can, in principle, be made only using sufficient number of high-resolution proxies of SST variability, such as fossil corals, in this region[6]. However, due to the insufficient number of direct ENSO proxies, the change of ENSO's amplitude has been often inferred indirectly from other proxies, notably the interannual variance of certain precipitation-sensitive proxies such as sediment fluxes [2, 4, 7, 8] and varve thickness[17, 39], in regions that are affected by ENSO teleconnection. This indirect inference may be valid under two conditions. (For simplicity, here, we ignore the issue related to the temporal resolution of the proxy). First, ENSO teleconnections remain stationary throughout times. Second, the proxy site is located in a region under strong ENSO impact; that is, the precipitation variability is highly correlated with ENSO such that most of its interannual variance is indeed caused by ENSO. Outside the region of strong ENSO impact, a significant part of the interannual variance in precipitation is contributed by local variability independent of ENSO[40]. Nevertheless, the amplitude of precipitation variability can still be correlated with that of ENSO

if the local response of interannual precipitation variability to a changing climate forcing, such as the orbital forcing, is similar to that of ENSO, rather than by teleconnection.

CCSM3 reproduces the ENSO teleconnetions reasonably well. A comparison of the correlation between the monthly time series of ENSO (Nino 3.4 SST) and interannual (1.5-7-yr) variability of precipitation for the present day in TRACE (Extended Data Fig.4c, 1-0ka) and the observation (Extended Data Fig.4d, HadISST and CPC Merged Analysis of Precipitation of 1981-2005) across the globe shows that the model captures the major features of the observed teleconnection, notably the positive correlation extending from the central equatorial Pacific to the South America coast and into the mid-latitude Northern Hemisphere, and the negative correlation surrounding the central-eastern equatorial Pacific, although the magnitude of correlation is somewhat underestimated in the model. In addition, a comparison of the ENSO teleconnection at different time periods in TRACE, for example, at the LGM (21-20ka, Extended Data Fig.4a), early deglaciation (16-15ka, Extended Data Fig.4b) and present (1-0ka, Extended Data Fig.4c), shows that the overall features of ENSO teleconnection remain largely unchanged.

In spite of statistically significant ENSO teleconnections globally, the region of strong ENSO impact is confined mainly in the core region of ENSO impact, from the central equatorial Pacific to the South America coast. This core region can be seen as the region with the correlation magnitude above 0.5 in the model (Extended Data Figs.4a-c). Precipitation variability as a proxy for ENSO amplitude changes in the core region is confirmed by calculation of the interdecadal amplitude correlation between precipitation variability and ENSO. The amplitude is calculated first in a 40-year window from the monthly time series filtered to the band of 1.5-7 years. The local response to slow external forcings, such as orbital and meltwater fluxes, is then filtered by subtracting its 200-year running mean. The high-pass interdecadal amplitude correlation (Extended Data Figs.4e-h) between the precipitation variance and ENSO variance in

the core region of ENSO impact, mainly in the equatorial Pacific to the South America coast, is positive similar to a previous work[26] and highly correlated (>0.6) in the central equatorial Pacific of Nino 4 and Nino 3.4 regions. This suggests that precipitation proxy records in the core region of ENSO impact can indeed be used to infer the change of ENSO amplitude reasonably well. In the very eastern equatorial Pacific and South America coast, such as Galapogos Islands and Ecuador, precipitation variability is also reasonable for inferring ENSO changes, as seen in Extended Data Figs.3a and 3b for the Holocene. Nevertheless, in these regions, the teleconnection correlation is not as large as in the central Pacific region (Extended Data Figs.4a-d) and the interdecadal amplitude correlation is also weak, usually smaller than 0.4 (Extended Data Figs.4e-h). Therefore, some failures of using precipitation variability to infer the correct trend of ENSO amplitude, for example, during the early deglaciation in the Galapogos Islands are possible (Extended Data Fig.3a).

Outside the core region of ENSO impact, the interdecadal amplitude correlation is usually small (Extended Data Figs.4e-h) and therefore precipitation variability can usually not be used to infer ENSO changes. However, the slow evolution of precipitation variance can still be correlated with that of ENSO. Extended Data Figs.5a-c show the correlation of the low-pass (200-year running mean) amplitude between precipitation variability and ENSO for different periods. The most striking feature is the high positive correlation in the central equatorial Pacific and South America coast, across all the periods, as in the interdecadal amplitude correlation (Extended Data Figs.4e-h). This is consistent with the implication of strong ENSO impact in this core region, as discussed above in Extended Data Fig.4.

Methods text 4: Further issues on model-data comparison of ENSO changes in the Holocene

Our model-data comparison of ENSO amplitude in the Holocene has focused on the qualitative aspects (Fig.1e). A quantitative model-data comparison would be much more challenging, because of the data interpretation and sample size as well as model deficiencies[41]. Overall, however, as in other models[20], our model underestimates the ENSO change in the Holocene, about 15%, against some reconstruction of SSTs of 50% or higher[3,21]. However, the small sample size[6,21] may not give a robust estimation of the ENSO amplitude trend[6]. Lake sediments[2,4] also show some large changes, but their interpretations remain illusive, especially for a quantitative comparison. ENSO amplitude is sensitive to the different measures such as the number of strongest events and the frequency of occurrence[41]. Thus, detailed quantitative model-data comparisons should be approached cautiously.

To illustrate the potential uncertainty related to the inherent irregularity of ENSO amplitude[16], as an example, we use the Monte Carlo method to test the trend of ENSO amplitude in the Holocene derived in the model as in the coral records of ref. 6. A model "fossil coral" record is simulated by a 30-year section of the monthly Niño 3.4 SST that is randomly selected between 7ka and 0ka. The ENSO amplitude is calculated as the standard deviation of the monthly SST in the frequency band of 1.5-7 years. The linear trend is then derived using a linear regression of the ENSO amplitudes of a set of 50 corals that are randomly selected between 7ka and 0ka. The probability density function (PDF) of the linear trend is then derived from an ensemble of 10,000 sets of 50-member corals (Extended Data Fig.6a, the red TRACE pdf profile). The null hypothesis PDF is derived from an ensemble of 10,000 sets of 50-member pseudo corals from a SST time series that is derived from the original Niño 3.4 SST time series in between 7 - 0ka after a random scrambling in time such that any linear trend is destroyed

(Extended Data Fig.6a, the red Null pdf profiles). It is seen that about half of the trends from the TRACE coral sets are statistically indifferent from zero at the 95% level. Therefore, consistent with ref. 6, it is difficult to detect a significant positive trend from a set of 50 corals of ~ 30-year length. To detect with high confidence a modest linear trend of ENSO amplitude of about 15%, as in TRACE and other models[20], either more or longer corals are needed. If the coral length is maintained at 30-year, but the coral member is increased to 200, the linear trend in TRACE can be detected significantly different from zero at 95% level (blue curves in Extended Data Fig.6a). If the coral members are increased to 1000, the positive linear trend can be detected at the 99% level (black curves in Extended Data Fig.6a).

The uncertainty of model-data comparison can also be seen in the evolution of the simulated ENSO amplitude (in the 100-year window, red in Extended Data Fig.6b) as compared with the most recent reconstructions from central Pacific corals[6] and Peruvian mollusks[21], all in reference to their respective late Holocene ENSO amplitude that is calculated as the average of the last millennium (1–0ka) (Extended Data Fig.6b). Although both the model and data show an increase of ENSO amplitude from the mid- to late Holocene, there are two differences between the model and data: first, the ENSO increase is less in the model (<20%) than in data (~50%), and, second, the model does not seem to simulate a mid-Holocene minimum. If the large ENSO intensification and mid-Holocene ENSO minimum are indeed robust features for the real world, the model-data discrepancies would imply substantial model deficiencies. However, these two observational features still remain uncertain, because of the high irregularity of ENSO, the sparse data sampling and data interpretation. For example, a reduction of the window length for ENSO amplitude from 100-year to 30-year in the model (blue line in Extended Data Fig.6b) to better represent the short length of corals would increase the spread of ENSO amplitude in the Holocene (10 - 0 ka after detrend) by 1.7 times; the increased spread implies a greater possibility

that the small number of coral records could have been influenced by the irregularity of ENSO. Using the spread of the annual range of SST along the Peru coast to infer ENSO amplitude[21] should depend on the phase-locking of ENSO with the annual cycle, and therefore could change with time if the phase-locking changes with time as in the simulation (Extended Data Fig.10). The ensemble spread of the SST reconstructions from $\delta^{18}O$ of planktonic G. ruber foraminifera in the eastern tropical Pacific[5] likely represents the total SST variability (Fig.1f), which is dominated by the annual cycle variance, rather than ENSO variance (Extended Data Figs.2b,c). Finally, ENSO center may shift between the central Pacific and eastern Pacific[21] (Extended Data Fig.2a), which could also reshape the patterns of ENSO-related precipitation anomalies that often form the basis of paleo-ENSO reconstructions. Ultimately, high-resolution paleoclimate data from ENSO centers of action must be expanded significantly to resolve these issues. In particular, we suggest that various types of temperature and precipitation-sensitive paleo proxy records from ENSO's center of action – the central equatorial Pacific (Extended Data Figs.2c,d) may provide particularly effective benchmarks for model simulations of ENSO variability.

Methods text 5: Estimating Ocean-Atmosphere Feedback

To examine the role of ocean-atmosphere feedback in ENSO evolution, we estimate ocean-atmosphere feedbacks in the tropical Pacific in TRACE by analyzing the surface ocean heat budget[23]. We first linearize the SST equation in the mixed layer as

$$\frac{\partial T}{\partial t} = Q - \frac{\partial(\overline{u}T)}{\partial x} - \frac{\partial(\overline{v}T)}{\partial y} - \frac{\partial(\overline{w}T)}{\partial z} - u\frac{\partial \overline{T}}{\partial x} - v\frac{\partial \overline{T}}{\partial y} - w\frac{\partial \overline{T}}{\partial z} \quad , \tag{1}$$

where the overbar denotes the annual mean climatology. Integration above the mixed layer depth (H_1) and then averaged over a region in the eastern equatorial Pacific, denoted in $\langle \ \rangle$, eqn. (1) can be approximated as

$$\frac{\partial \langle T \rangle}{\partial t} = \langle Q \rangle - \left(\frac{(\overline{u}T)_{EB} - (\overline{u}T)_{WB}}{L_x} + \frac{(\overline{v}T)_{NB} - (\overline{v}T)_{SB}}{L_y} \right)$$
$$- \left\langle \frac{\partial \overline{T}}{\partial x} \right\rangle \langle u \rangle - \left\langle \frac{\partial \overline{T}}{\partial z} \right\rangle \langle H(\overline{w})w \rangle + \left\langle \frac{\overline{w}}{H_1} \right\rangle \langle H(\overline{w})T_{sub} \rangle$$

(2)

where $H(x)=1$ if $x>=0$ and $H(x)=0$ if $x<0$, is the Heaviside step function. Here, all the terms are derived similar to ref. 23, except the second term, which represents the mean advection, with the subscripts "EB", "WB", "NB" and "SB" denoting the average along the eastern, western, northern and southern boundaries of the region, respectively, L_x and L_y as the longitudinal and latitudinal widths of the region, respectively. The damping coefficients associated with the negative feedback of the surface heat flux and mean advection are derived as the regression coefficients with SST as

$$\langle Q \rangle = -\alpha_s \langle T \rangle, \quad -\left(\frac{(\overline{u}T)_{EB} - (\overline{u}T)_{WB}}{L_x} \right) = -\alpha_{MU} \langle T \rangle, \quad -\left(\frac{(\overline{v}T)_{NB} - (\overline{v}T)_{SB}}{L_y} \right) = -\alpha_{MV} \langle T \rangle; \quad (3a)$$

The atmospheric response sensitivity to the eastern Pacific SST is estimated approximately in the regression coefficient μ_a between the cross-basin mean atmospheric wind (stress, $[\tau_x]$) and the eastern Pacific SST as

$$[\tau_x] = \mu_a \langle T \rangle; \quad (3b)$$

The entrainment temperature is proportional to the depth of the local thermocline $\langle h \rangle$ as

$$\langle H(\overline{w})T_{sub} \rangle = a_h \langle h \rangle; \quad (3c)$$

Finally, the oceanic response sensitivities to the wind stress are regressed as

$$\langle h \rangle - \langle h \rangle_W = \beta_h [\tau_x], \quad \langle H(\overline{w})w \rangle = -\beta_W [\tau_x], \quad \langle u \rangle = \beta_u [\tau_x]; \quad (3d)$$

for the thermocline slope, upwelling and zonal current, respectively. Here, $\langle h \rangle_W$ is the thermocline depth in the western equatorial Pacific. With all the regression coefficients in (3a-d), eqn. (2) can be approximated as

$$\frac{\partial \langle T \rangle}{\partial t} \approx R \langle T \rangle, \tag{4}$$

where the total feedback parameter, or the Bjerkness index (BJ index), is

$$R = -\alpha_s - \alpha_{MA} + \mu_a \beta_u \langle -\overline{T}_x \rangle + \mu_a \beta_w \langle -\overline{T}_z \rangle + \mu_a \beta_h \left\langle \frac{\overline{w}}{H_1} \right\rangle a_h \tag{5}$$

The BJ index consists of five feedbacks terms, which are, in order, the surface heat flux feedback, the mean advection feedback ($\alpha_{MA} = \alpha_{MU} + \alpha_{MV}$), the zonal advection feedback, the local upwelling feedback, and the thermocline feedback. The last three feedbacks are all proportional to the atmospheric response sensitivity (μ_a), and each is further proportional to its own oceanic response sensitivities ($\beta 's$).   Here, we choose: H_1 as 50-m, w and $\overline{w}$ as the anomalous and climatological upwelling at 50-m, h approximately as the heat content anomaly, which is derived as the column-weighted temperatures at the three model levels of 4-m (surface), 56-m and 149-m, $\overline{T}_z$ as the difference of climatological temperatures between the surface and 100-m. All the climatology variables are derived as the time-mean over a sliding window of 100 (or 300) years, while the anomalies are the monthly deviations from the climatological seasonal cycle.

For the eastern part of the equatorial Pacific (180°W-80°W, 5°S-5°N), which is the region of dominant ENSO variability (Extended Data Fig.2a), the BJ index is negative, mainly due to the mean (meridional) advection feedback (Extended Data Fig.7b). The negative BJ index indicates that ENSO is a stable mode maintained by stochastic forcing in CCSM3, as in most CGCMs[42]. Almost all the feedbacks tend to follow the orbital forcing in the southern subtropics (Fig.2), with the magnitude of the feedback decreasing towards the early Holocene, but

increasing towards both late Holocene and LGM. There is also significant millennial variability reminiscent of the meltwater forcing during the early deglaciation, especially in the upwelling feedback. The dominant role of orbital forcing for the slow evolution throughout the 21,000 years is also confirmed by the similar BJ indices in TRACE and ORB runs (Fig.2d), and the dominant role of the upwelling feedback in TRACE (Extended Data Fig.7b) and ORB (not shown). Finally, the mean advection feedback also shows an abrupt increase (less negative) at ~14ka due to the retreat of the ice sheet, a point to be returned later.

The BJ index is consistent with the ENSO amplitude over most of the Holocene, both increasing from 8ka towards the late Holocene (Figs.2b and d, or Extended Data Fig.7a). Therefore, ENSO intensification in the Holocene can be interpreted from the linear instability perspective as being caused by increased ocean-atmosphere feedback. The increase of BJ index is dominated by the upwelling feedback, with a minor contribution from the thermocline feedback; their sum overwhelms the decrease (more negative) of the two negative feedbacks (Extended Data Fig.7b), leading to a modest increase of the total feedback and, in turn, ENSO amplitude (Extended Data Fig.7a). The increases of the three positive feedbacks are contributed by a common atmospheric response sensitivity (μ_a, Extended Data Fig.8a) as well as their respective oceanic response sensitivities ($\beta\,'s$) (Extended Data Figs.8b,c,d).

In more details, the upwelling feedback is further enhanced significantly by the intensified stratification (Extended Data Fig.8f) which is caused by the precessional forcing of the subtropical South Pacific[12]. The weaker stratification in the early Holocene is caused by the precessional forcing (Extended Data Fig.9a) on the subtropical South Pacific, where the increased insolation in austral winter warms the surface water in winter (Extended Data Fig.9b) and then the subsurface thermocline all year round through late winter subduction (Extended Data Fig.9c); the warmer subduction water is eventually transported into the equatorial

thermocline, warming the subsurface and reducing the stratification (Extended Data Fig.9d). Our further calculations with various domain choices for the eastern Pacific show that the dominant contribution of the upwelling feedback is robust. The small zonal advection feedback in Extended Data Fig.7b is caused partly by a small climatological SST zonal gradient averaged across the region, i.e. $\langle -\bar{T}_x \rangle$, which is proportional to the small difference of climatological SST between the eastern and western boundaries of the eastern Pacific domain chosen here (180$^{\rm o}$W vs. 80$^{\rm o}$W). With other choices of the domain, such as the Niño3.4 domain (170$^{\rm o}$W vs 120$^{\rm o}$W), the increase of the zonal advection feedback in the Holocene is larger, but still smaller than that of the upwelling feedback.

In contrast to the Holocene, during the deglacial period (~18ka-8ka), the BJ index does not co-vary with the ENSO amplitude for millennial variability, for example, around the periods of HS1 and YD. Therefore, the millennial modulation of ENSO cannot be attributed to the change of feedbacks. The millennial modulation of ENSO varies out of phase with the seasonal cycle and therefore can be attributed to the interaction with the seasonal cycle through the nonlinear mechanism of frequency entrainment[27], with the equatorial seasonal cycle altered by the meltwater water discharge through the AMOC[26]. The response sensitivities, the climatological states and in turn the three positive feedbacks (Extended Data Fig.7b) all evolve in more complex patterns during deglacial than in the Holocene. The heat flux negative feedback exhibits only modest changes. The most striking change is an abrupt reduction (less negative) of the mean advection damping at ~14ka (Extended Data Fig.7b), which is contributed mainly by the mean zonal advection. This abrupt weakening of the mean (zonal) advection damping is caused by the large retreat of ice sheet at 14ka, and is consistent with the abrupt increase of ENSO amplitude (Fig.3a) and mean (zonal) advection feedback (similar to that in Extended Data Fig.7b) in the ICE run at ~14ka. The abrupt intensification of ENSO at ~14ka in ICE is caused

by the frequency entrainment through the sudden decrease of annual cycle (Fig.3b). The annual cycle reduced associated with an annual mean SST in the eastern Pacific more symmetric about the equator, which is forced by the atmospheric teleconnection response to the large retreat of the North America ice sheet at ~14ka. The ice sheet retreat induces a northward migration of the atmospheric westerly jet over the North Atlantic, an increase of surface easterly in the tropical North Atlantic and in turn tropical eastern Pacific; the ice sheet retreat also changes the atmospheric stationary wave response, which leads to a cooling and an sea ice expansion over the subpolar North Pacific, and also an intensified trade wind in the eastern Pacific. Either way, the intensified trade wind in the eastern Pacific propagates equatorward through ocean-atmosphere coupling, leading to a cooling north of the equator, which reduces the SST gradient northward and leads to an annual mean SST more symmetric about the equator in the eastern Pacific. The detailed mechanism of the ENSO response in ICE is beyond the scope of this study and will be presented elsewhere.

Methods References

31. Berger, A., Long-term variations of daily insolation and quaternary climatic changes *J. Atmos. Sci*. **35**, 2362-2367 (1978).

32. McManus J. et al., Collapse and rapid resumption of Atlantic meridional circulation linked to deglacial climate changes. *Nature* **428**, 834-837 (2004)

33. Joos, F. & Spahni, R., Rates of change in natural and anthropogenic radiative forcing over the past 20,000 years. *Proc Nat Aca Sci*, **105**, 1425-1430 (2008).

34. Collins W. et al., The community climate system model version 3 (CCSM3). *J. Clim.,* **19,** 2122-2143 (2006).

35. Peltier, W., Global glacial isostasy and the surface of the ice-age earth: the ICE-5G (VM2) model and GRACE. *Annu. Rev. Earth Planet. Sci.* **32**, 111-149 (2004).

36. He, F., Simulating transient climate evolution of the last deglaciation with CCSM3. *Ph.D thesis, Dept. Atmos. & Oceanic Sci., Univ. Wisconsin-Madison*. 161 pp (2011).

37. He F. et al, Northern Hemisphere forcing of Southern Hemisphere Climate during the last deglaciation. *Nature*, **494**, 81-85 (2013).

38. Deser C. et al, Tropical Pacific and Atlantic climate variability in CCSM3. *J. Clim.*, **19**, 2451-2481 (2006)

39. Rittenour, T., Brigham-Grette J. & Mann M., El Niño-like climate teleconnections in New England during the late Pleistocene. *Science*, **288**, 1039-1042 (2000).

40. McGregor S. et al., Inferred changes in El Niño-Southern Oscillation variation over the past six centuries. *Clim. Past*, **9**, 2269-2284 (2013)

41. Brown J. et al, Issues in quantitative model-proxy data comparisons, *Paleoceanography*, **23**, PA3202 (2008).

42. Kim, S. & Jin, F., An ENSO stability analysis: Part II. Results from twentieth and twenty-first century simulations of the CMIP3 models. *Clim. Dyn.*, DOI 10.1007/s00382-010-0796-0 (2010)

Extended Data Legends
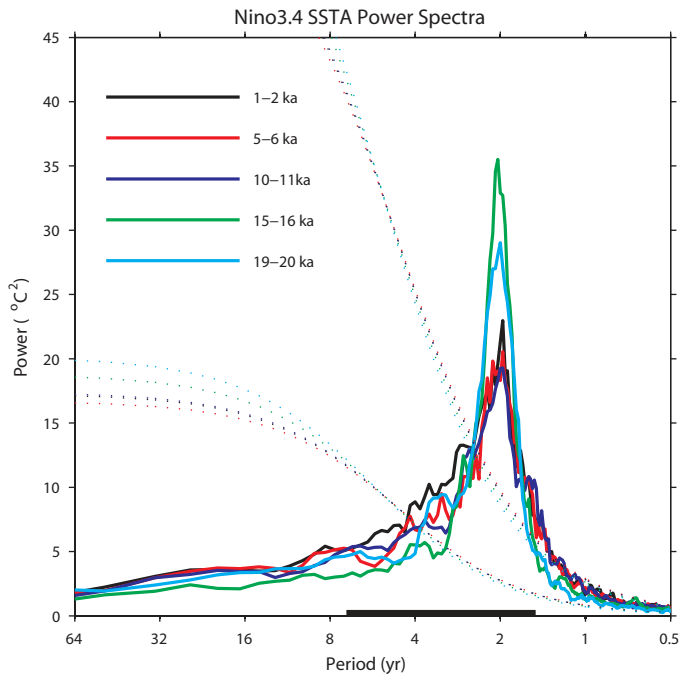
Extended Data Fig. 1: Power spectrum of ENSO: Power spectra of Nino 3.4 monthly SST variability in TRACE (after removing the annual cycle) in five 1000-year windows: 1-2 ka, 5-6 ka, 10-11ka, 15-16ka and 19-20ka. The spectral peak remains at ~2-year, but with different intensity. For each spectra, the 95% cut-off level and the corresponding red noise curve are also plotted (in dotted lines). The black bar at the bottom shows the 1.5-7 year band that used for the calculation of ENSO variance.
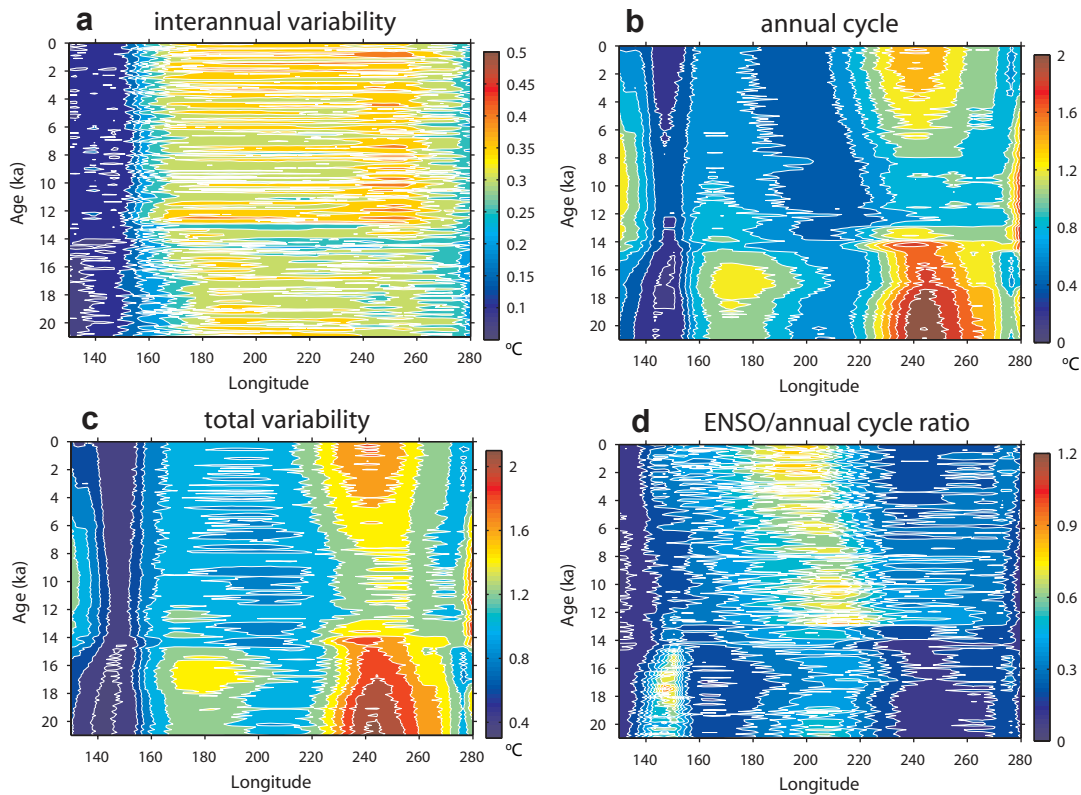
Extended Data Fig.2: Evolution of ENSO and annual cycle along the equator: Evolution of the amplitudes (standard deviation in 100-year window) of (a) interannual (1.5-7 year) variability, (b) annual cycle of SST, (c) total variability (<7-year) and (d) the ratio of the amplitudes of interannual over annual cycle along the equatorial Pacific (5°S-5°N) in TRACE. The total variability is dominated by the annual cycle, except in the central-eastern Pacific, where ENSO becomes dominant. This occurs because ENSO variability exhibits a broad pattern from central to eastern Pacific, while the annual cycle is strong along the eastern boundary and decays rapidly towards the central Pacific.
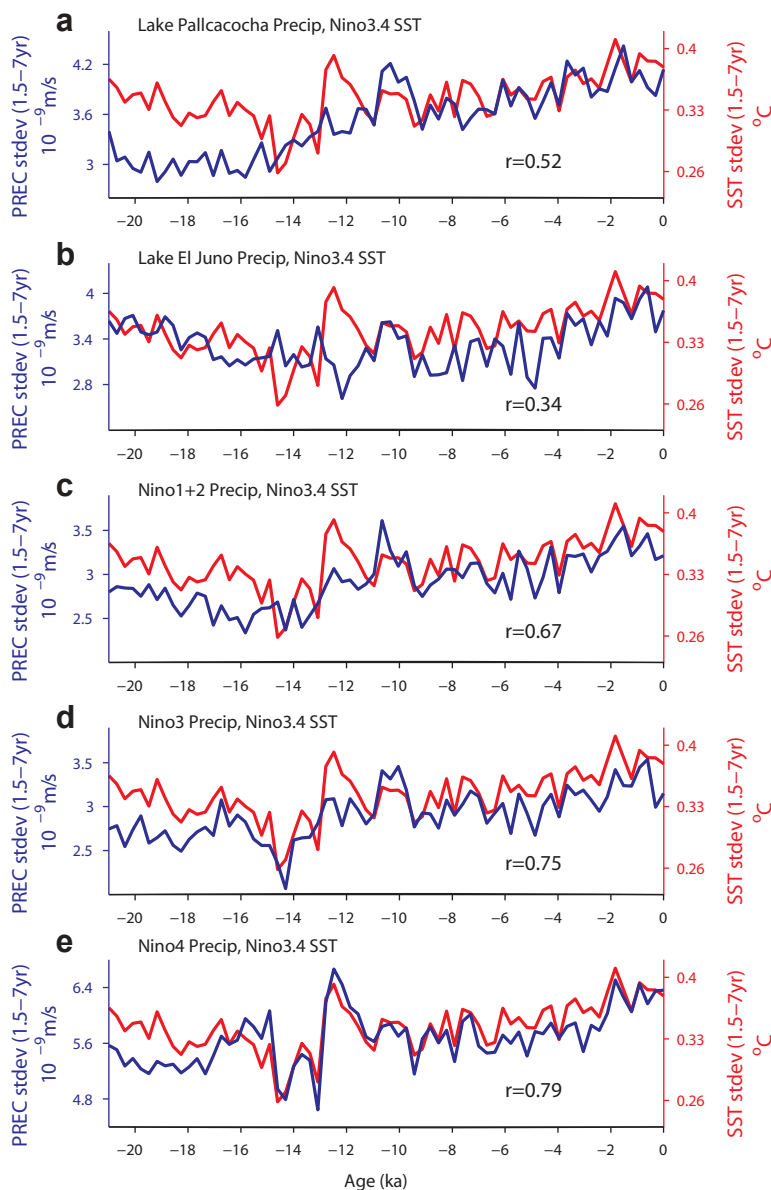
Extended Data Fig.3: Evolution of variability amplitude: Evolution of the amplitude of interannual (1.5-7-yr) variability of precipitation (blue) in TRACE in (a) Ecuador[2], (b) Galapogos Islands (Lake El Juno)[7], (c) Nino1+Nino2, (d) Nino 3 and (e) Nino 4 (locations marked in Extended Data Figs.4, 5). All the anomalies are the monthly data with a 3-month running mean filtered to the 1.5-7-year band. The amplitude is calculated as the standard deviation of the 1.5-7-year band-passed monthly time series in succeeding 300-year windows. For reference, the amplitude of Nino3.4 SST interannual variability is also plotted in each panel

(red). The correlation between each curve and the amplitude of ENSO is also calculated. All correlations are highly significant with p-values smaller than 0.01 (with a sample size of 70).
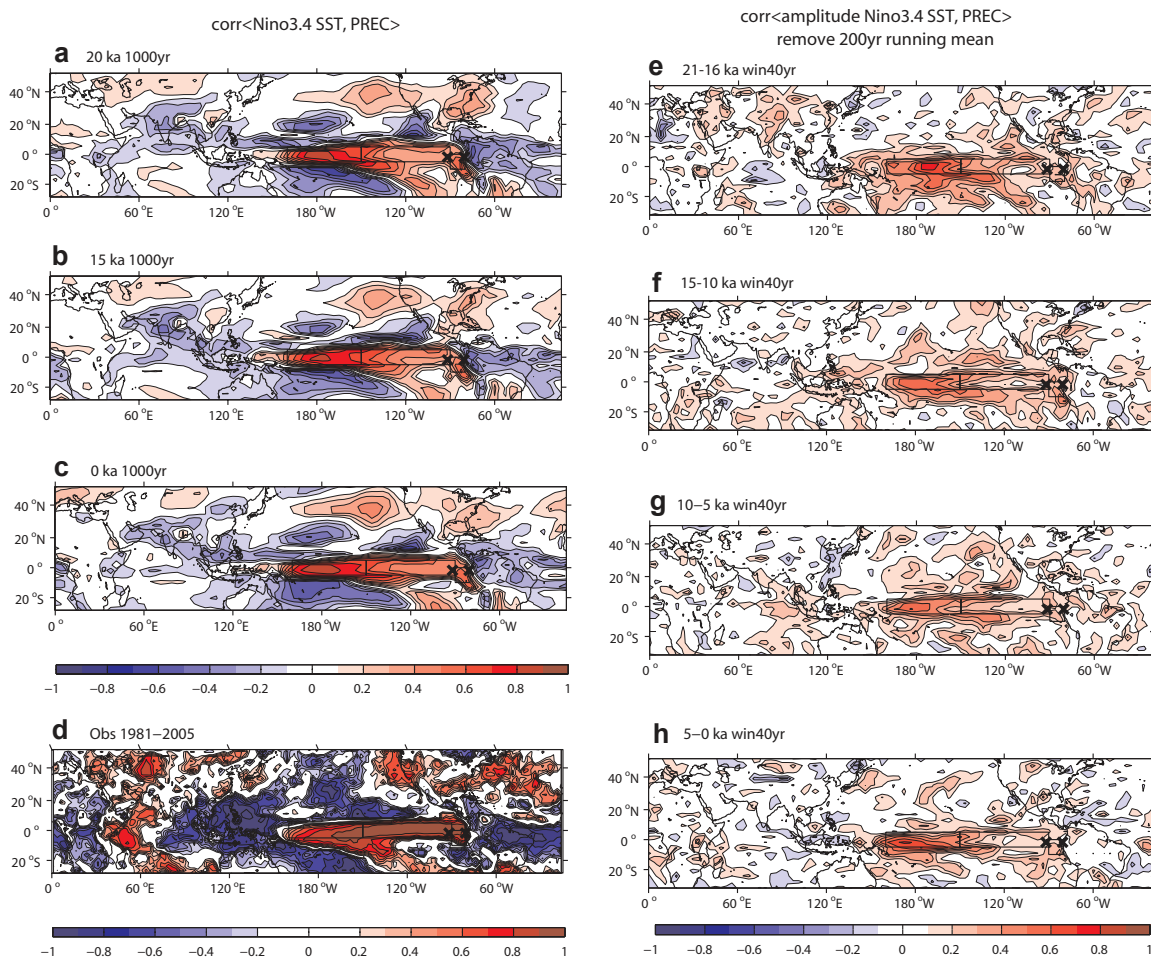
Extended Data Fig.4: Correlation map between ENSO and precipitation: (Left) Map of time series correlation of interannual (1.5-7 yr) variability between monthly Nino 3.4 SST and precipitation during a) 21-20ka, (b) 16-15ka, c) 1-0ka in TRACE and (d) the present observation (1981-2005). (Right) Map of interdecadal amplitude correlation between interannual ENSO (Nino 3.4 SST) and precipitation variability during (e) 21-20ka, (f) 15-14ka) and (g) 1-0ka. All the anomalies are the monthly data with a 3-month running mean after filtered to the 1.5-7-year band. For (e-g), the amplitude is calculated as the standard deviation in a 40-year window and the detrended amplitude in the 1000-year period is used to calculate the amplitude correlation.

The 2 black crosses indicate the region of proxy observation in Galapogos Islands[7] and Ecuador coast[2], respectively, and the three black boxes denote the regions of Nino1+2, Nino 3 and Nino 4 discussed in Extended Data Fig.3. Colors in correlations indicate regions where the correlation is significant more than 99% level.
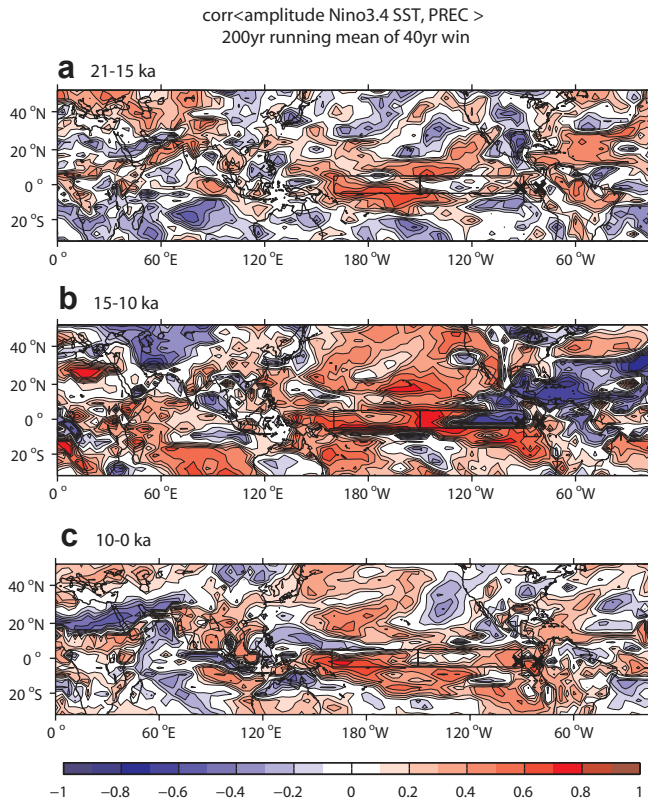

Extended Data Fig.5: Correlation between the amplitudes of ENSO and precipitation variability. Map of the correlation between the 200-year running amplitudes of interannual ENSO and precipitation variability during (a) 21-15ka, (b) 15-10ka) and (c) 10-0ka. The 2 black crosses indicate the region of proxy observation in Galapogos Islands[7] and Ecuador coast[2], respectively, and the three black boxes denote the regions of Nino1+2, Nino 3 and Nino 4 as discussed in Extended data Fig.3. The result will be similar if the amplitude is calculated directly

using 300-year window as in Extended data Fig.3. Colors in model correlations indicate regions where the correlations are significant more than 99% level.
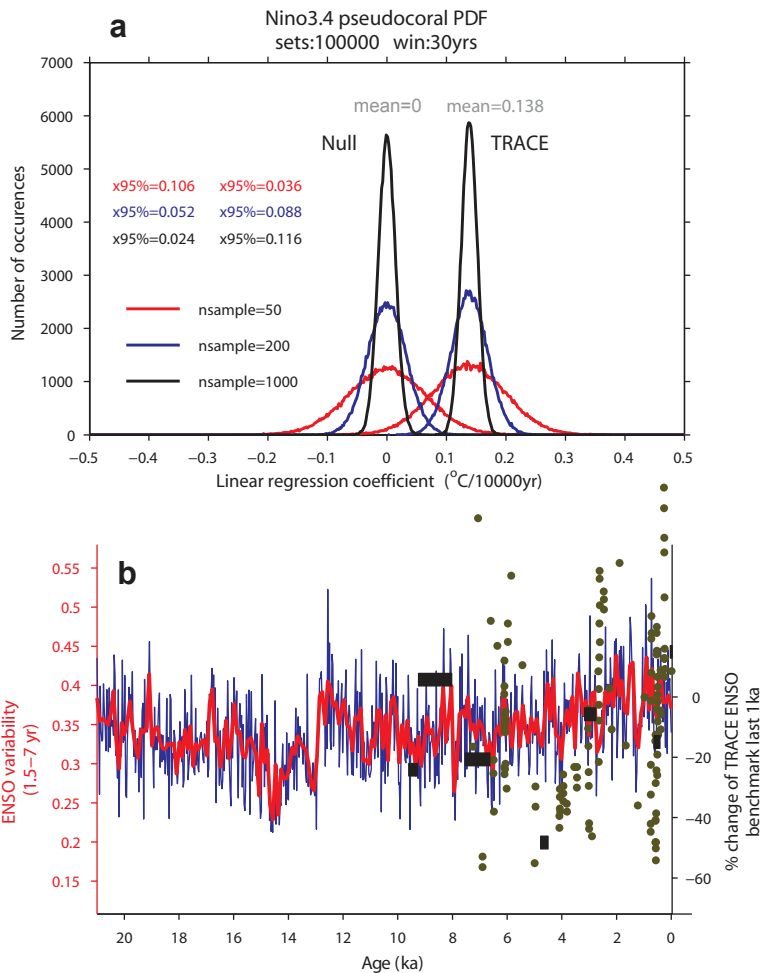

Extended Data Fig.6: Uncertainty for ENSO model-data comparison: (a) Detecting trend of ENSO amplitude in "pseudo corals". Histogram of Holocene (7-0ka) linear trends of ENSO amplitude derived from 30-year "pseudo coral" records of the Nino3.4 SST in TRACE. A linear trend (regression coefficient) is derived from the ENSO amplitudes of a random set of 50 (red) "corals", with each ENSO amplitude as the standard deviation of the interannual (1.5-7 years) SST variability of a 30-year section of "coral record". The PDF on the right (marked with TRACE) is derived from the linear trends of 100,000 randomly formed sets of coral records, while the PDF on the left (marked with Null) is the null hypothesis of no trend in ENSO

amplitude, and is derived from the linear trend of a time series after random scrambling of the Nino3.4 SST. Two additional PDFs are derived with the number of corals increased to 200 (blue) and 1000 (black) in each set. The right-side one-tail 95% significance levels are 0.106 (red), 0.052 (blue) and 0.024 (black) for the Null hypothesis and the left-side one-tail 95% significance levels are 0.036 (red), 0.088 (blue) and 0.116 (black) for TRACE. With 50 corals, the trend in TRACE can't be identified at the 95% level because the significance level in TRACE is below that of NULL (0.036< 0.106); with 200 corals, the trend can be identified at 95% level because the significance level of TRACE is beyond that of NULL (0.088 > 0.052); with 1000 corals, the 95% significance levels become well beyond the NULL (0.116 >> 0.024), implying highly significant trend of ENSO strengthening in the Holocene. (b) ENSO amplitude in TRACE in 100-year window (red thick line, same as in Fig.1e) and 30-year window (blue thin line) (both in the left axis) as well as the ENSO variance reconstructed from corals in the central Pacific[6] (dark green dots) and from the variance of annual SST range from mollusk shells along Peru coast[21] (black horizontal bars). The two data are plotted in changes relative to the present ENSO amplitude (in the right axis), which is then rescaled with the model ENSO amplitude such that the relative change of model ENSO amplitude can also be scaled in the right axis. All the model and proxy data are aligned and referenced to their last millennium average (1 to 0 ka).
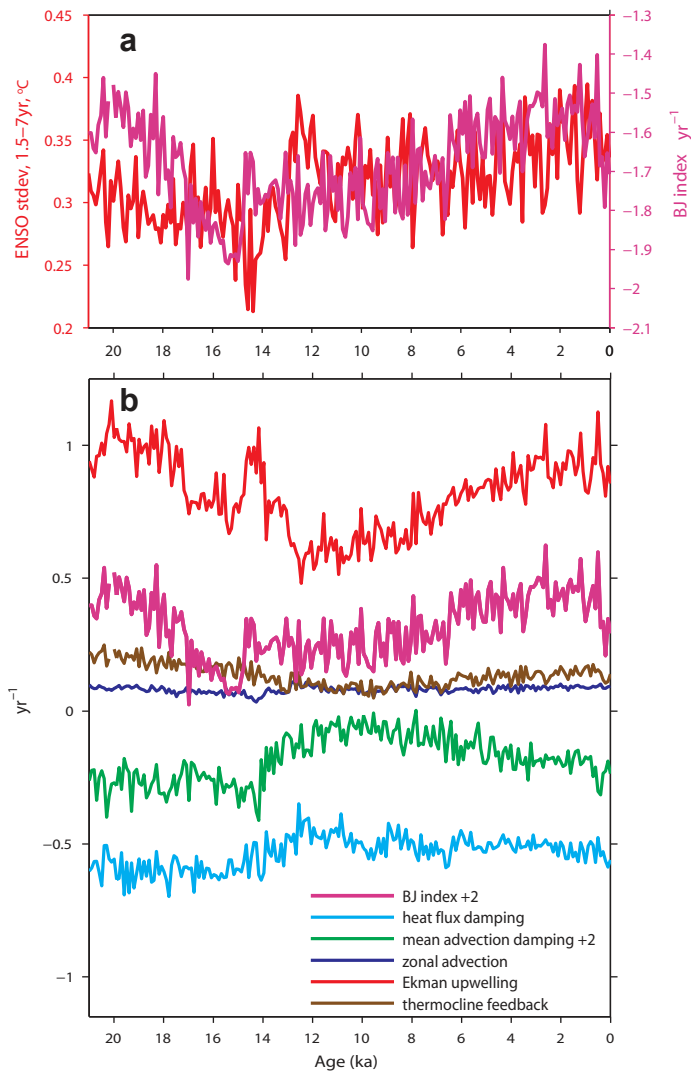
Extended Data Fig.7: Evolution of BJ-index and its components: Evolution of ocean-atmosphere feedbacks in the eastern equatorial Pacific region (180E-80W, 5S-5N) for interannual (1.5-7-yr band) ENSO variability in 100-year windows in TRACE. (a) ENSO amplitude (red) and the BJ index (purple, offset +2); (b) The two negative (damping) feedbacks: surface heat flux feedback (cyan), mean advection feedback (green, offset by +2), and three positive feedbacks: zonal advection feedback (blue), Ekman upwelling feedback (red) and thermocline feedback (yellow), as well as the (sum) total feedback (BJ index, purple). The ENSO amplitude largely follows the BJ index (an increasing trend) in the Holocene, but not in

the deglaciation, suggesting the dominant role of ocean-atmosphere feedback for ENSO

intensification in the Holocene, but not for millennial variability in deglaciation.
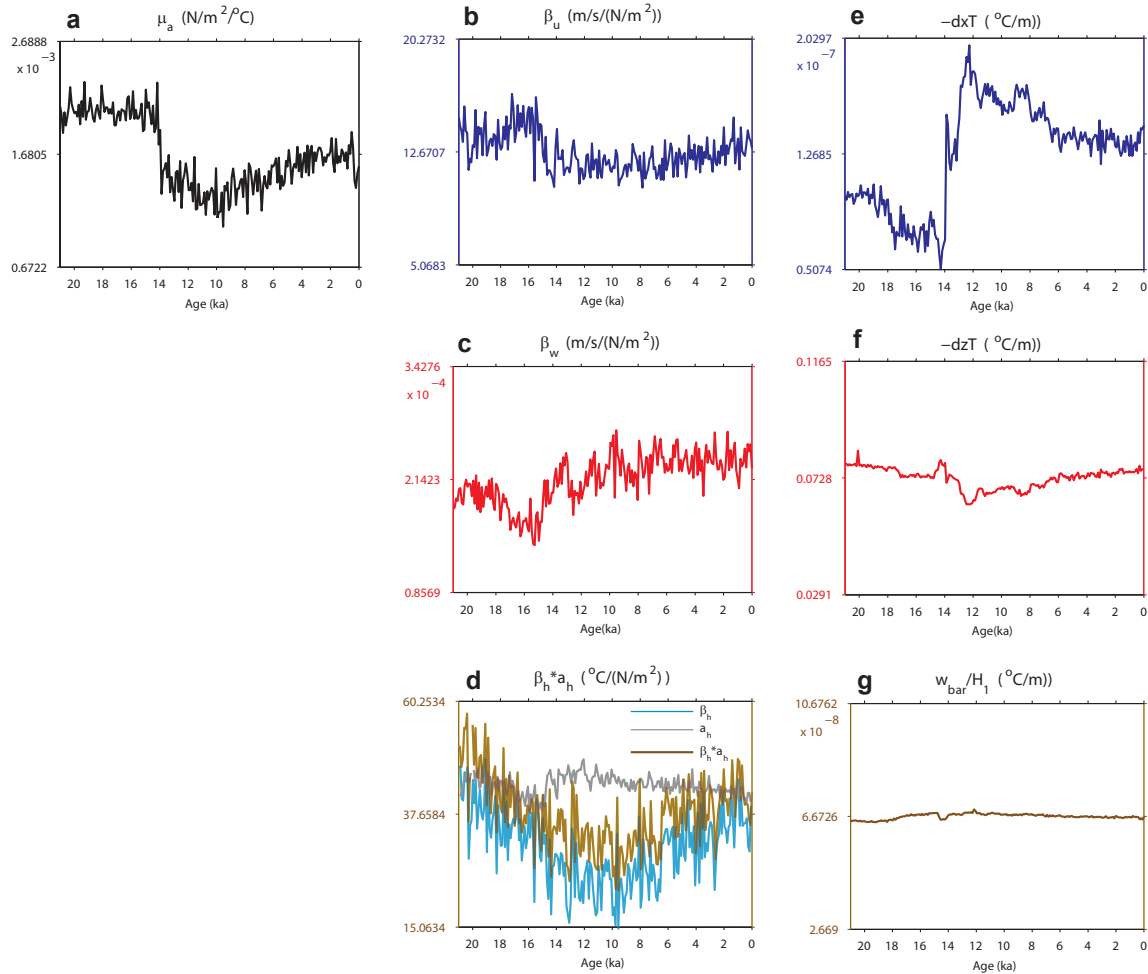
Extended Data Fig.8: Evolution of feedback coefficients: Response sensitivity and mean state

for interannual variability in the eastern equatorial Pacific region (170E-80W, 5S-5N) in TRACE.

(a) atmospheric response sensitivity to SST, (b) zonal current response sensitivity to wind stress,

(c) upwelling response sensitivity to wind stress, (d) thermocline response sensitivity to wind

stress ($\beta_h a_h$, brown), β_h (cyan) and a_h (grey), (e) mean zonal SST gradient, (f) mean stratification,

(g) mean upwelling. In (a)-(d), each curve is plotted in the same relative scale such that their

variation can be compared directly: The scale of a variable y ranges from median (y)-0.6|mean(y)| to median (y)+0.6|mean(y)|.
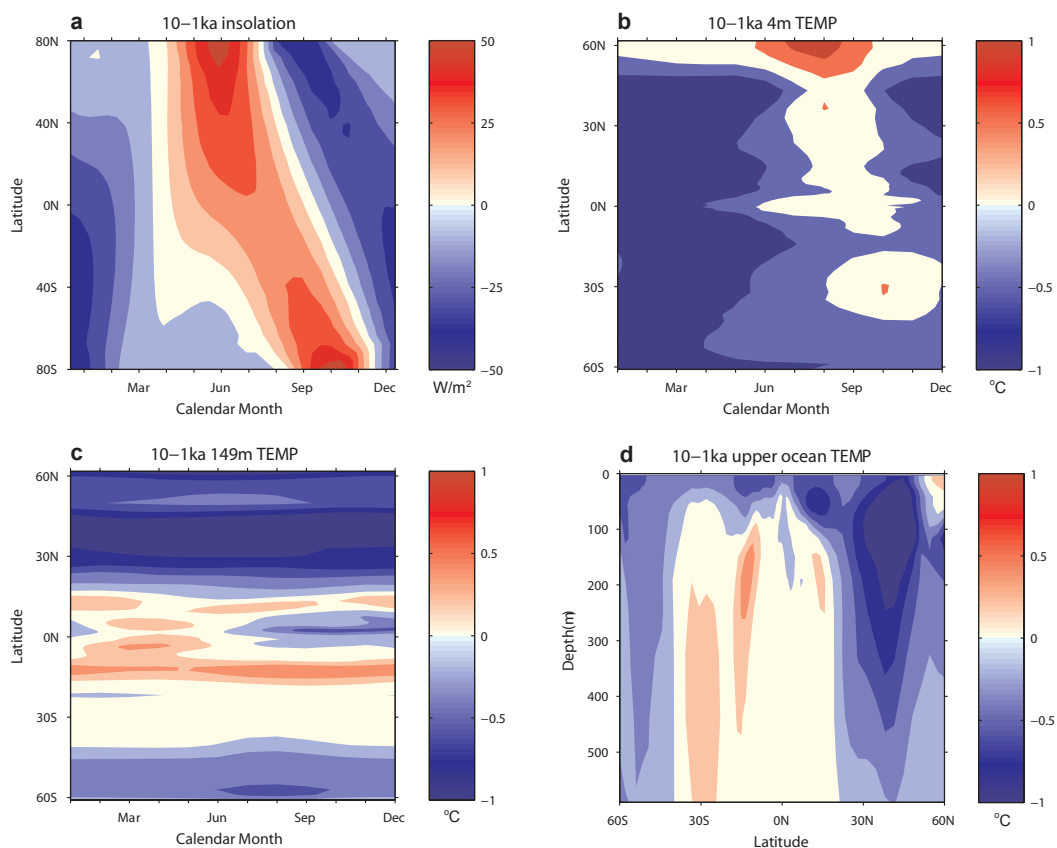
Extended Data Fig.9: Response of equatorial thermocline in the Holocene: The annual cycle of the 10ka - 1ka difference of (a) insolation, and South Pacific temperature (°C) at (b) the surface and (c) 149-m depth for different latitudes in TRACE. (d) shows the zonal mean annual mean temperature difference in the upper ocean of the South Pacific (180W-100W). In the subtropical South Pacific (40S-10S), the insolation warming in austral winter (in (a)) leads to a SST warming in austral winter-spring (in (b)), which is then ventilated into the subsurface thermocline as a warming throughout the year (in (c)), and eventually into the equatorial thermocline (in (d)), reducing the stratification there.
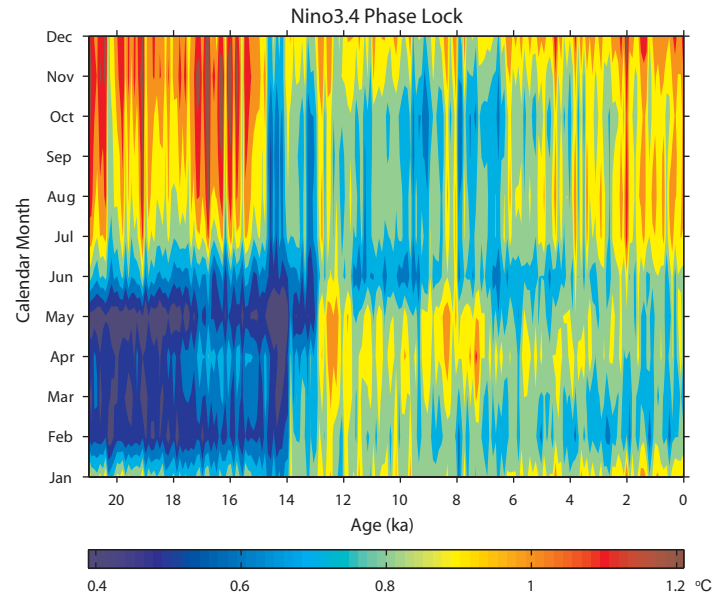
Extended Data Fig.10: Phase-locking of ENSO: Evolution of phase locking of Nino 3.4 SST interannual variability as a function of the calendar month in 100-year windows. The peak of ENSO anomaly is locked strongly to boreal winter in early deglaciation; this se-locking is weakened towards the early Holocene, but re-emerges towards late Holocene.